Supporting Information: Controlling Particle Dynamics in Dead-End Channels via Tunable Boundary Effects

Langqi Xing[1] and Xiaoyu Tang[12*]

Contents

*Email: x.tang@northeastern.edu
[1]Department of Mechanical and Industrial Engineering, Northeastern University, MA 02115, United States
[2]Department of Chemical Engineering, Northeastern University, MA 02115, United States

1 Particle and Boundary Wall Properties

One particle and two wall boundaries were used in this study. The general information for these materials is given below.

Table S1: General property of the particle used in experiments.

Particle Surface	Diameter (µm)	Abs./Em. (nm)
Carboxylate	0.955 ± 0.04	480/520

Table S2: General property of wall materials used in experiments.

Wall Surface	Viscosity (mPa·s)	Mixing Ratio	Curing Time (s)
PDMS	3500	10:1	7200
NOA-81	300	-	20

1.1 Zeta Potential of PS-COOH Particle

Zeta potential of PS-COOH particles was measured as a function of NaCl concentration and is shown in Fig. S1. The data were fit using a logarithmic dependence,

$$\zeta_{PSCOOH}(C) \;=\; a_p \;+\; b_p \log_{10}(C), \tag{S1}$$

where C is the NaCl concentration and ζ_{PSCOOH} is in volts. For the PS particle fit used in this work (with C in M),

$$\zeta_{PSCOOH}(C) \;=\; -47.92 \times 10^{-3} \;+\; 0.705 \times 10^{-3} \log_{10}(C). \tag{S2}$$

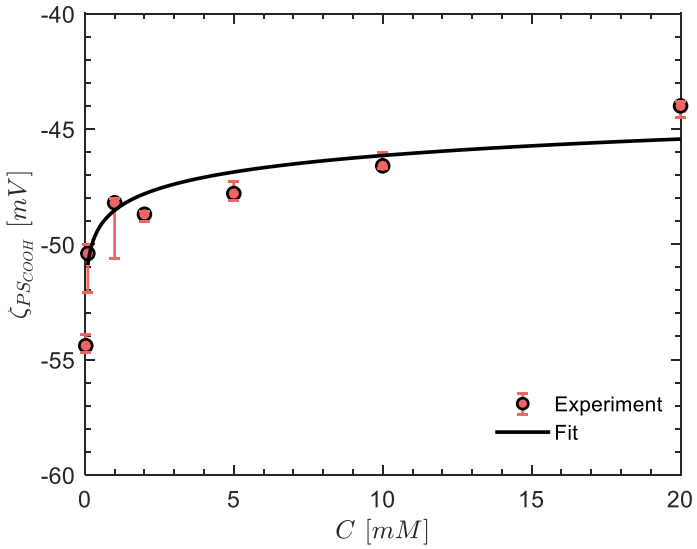

Fig. S1: Zeta potential of PS-COOH particles as a function of NaCl concentration (C). The solid line indicates the logarithmic fit used in the theoretical analysis (Eq. S2). Error bars represent measurement variability across repeats.

1.2 Zeta Potential of Boundary Wall Materials (PDMS, NOA-81 glue, and glass)

The surface zeta potential of each channel boundary material (PDMS, NOA-81 glue, and glass) was characterized as a function of NaCl concentration C (Fig. S2). Over the tested salt range, the results were described by a logarithmic dependence,

$$\zeta_{\text{wall}}(C) \;=\; a_{\text{wall}} \;+\; b_{\text{wall}}\,\log_{10}(C)\,, \tag{S3}$$

with ζ_{wall} in mV and C in M.

For PDMS, the fit implemented in the model as discussed in Akdeniz's paper [4] was

$$\zeta_{\text{PDMS}}(C) \;=\; -6.27 \;+\; 29.75\,\log_{10}(C)\,, \tag{S4}$$

where ζ_{PDMS} is in mV and C is in M.

For the NOA-81 UV glue, the experimental data from the methods in Section 3.5 was fitted from Kirby et al.[1]:

$$\zeta_{\text{glue}}(C) \;=\; -13.76 \;+\; 3.19\,\log_{10}(C)\,, \tag{S5}$$

For the glass substrate, the data was obtained using Gu's paper [9] and fitted with Eq.S3,

$$\zeta_{\text{glass}}(C) \;=\; 16.667 \;+\; 11.98\,\log_{10}(C)\,, \tag{S6}$$

where ζ_{glass} is in mV and C is in M.

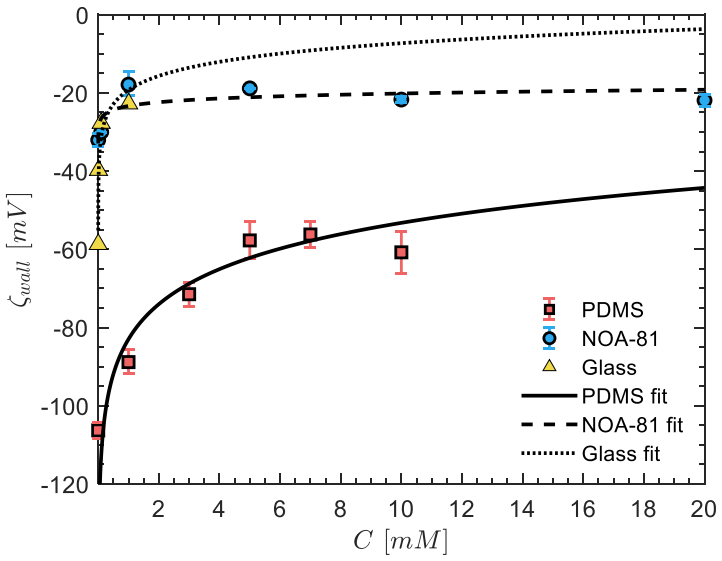

Fig. S2: Surface zeta potential ζ_{wall} of PDMS, NOA-81 (UV glue), and glass as a function of NaCl concentration (C). Solid/dashed/dotted curves indicate the logarithmic fits used as electrokinetic inputs for theoretical predictions (Eqs. S3–S6). Error bars represent measurement variability across repeats.

2 Experimental Error Sources

Particle detection and calculation methods in custom MATLAB codes can introduce several types of errors. Understanding these sources of error is crucial for the accurate interpretation of velocity measurements.

2.1 Pixel Resolution Limitation

The precision of particle position detection is fundamentally limited by the finite size of camera pixels. This positional uncertainty can be quantified using the equation[2]:

$$(\Delta U)^2 = \left(\frac{\Delta x_{i+1}}{\Delta t}\right)^2 + \left(\frac{\Delta x_i}{\Delta t}\right)^2 = 2\left(\frac{\Delta x}{\Delta t}\right)^2 \tag{S7}$$

where ΔU represents the velocity uncertainty, Δt is the image time frame, and Δx is the position uncertainty, calculated from the micron-to-pixel ratio. At a frame rate of 10 fps, the velocity uncertainty is $0.5\,\mu$m/s, and at 1 fps, it reduces to $0.05\,\mu$m/s. Thus, the effect of pixel size is more pronounced at lower frame rates but remains a relatively minor source of error under typical conditions.

2.2 Influence of Brownian Motion

For particles with very small velocities (less than $1\,\mu$m/s), Brownian motion can significantly affect the accuracy of velocity measurements. The relative error due to Brownian motion is described by[3]:

$$\epsilon_x = \frac{1}{\bar{U}}\sqrt{\frac{2D_p}{\Delta t}} \tag{S8}$$

Here, $\bar{U}$ is the average particle velocity, and D_p is the particle diffusivity. This formula establishes that error increases inversely with particle velocity and directly with particle diffusivity. For frame rates of 10 fps and 1 fps, the corresponding critical velocity limits are $1.7\,\mu$m/s and $0.96\,\mu$m/s, respectively.[4]

2.3 Response Time in Low Viscosity

The dynamic response of particles to sudden accelerations, particularly in low-viscosity environments, introduces another layer of complexity[3]:

$$\tau_p = \frac{d^2\rho_p}{18\eta} \tag{S9}$$

where d is the particle diameter, ρ_p is the particle density, and η is the fluid viscosity. With a response time of only 78 ns, this factor is negligible compared to typical image frame times, ensuring that it does not affect the particle velocity analysis.

3 Analysis of NaCl Concentration Profile

As NaCl diffuses from regions of high concentration to low concentration, it establishes a transient solute concentration gradient within the dead-end channel. This gradient is crucial because it drives particle diffusiophoresis and wall diffusio-osmosis, inducing movement of particles and fluid, respectively. The local solute concentration also influences electrokinetic parameters like the zeta potentials of particles and channel walls, affecting the transport phenomena.

We theoretically determined the sodium chloride (NaCl) concentration profiles in the dead-end microchannel by solving the one-dimensional diffusion equation (Eq. S10). [5] As shown in Fig. S3, the concentration field $C(x,t)$ along the channel axis $x \in [0, L]$ evolves in time according to

$$\frac{\partial C}{\partial t} = D \frac{\partial^2 C}{\partial x^2}, \tag{S10}$$

where D is the solute diffusivity. The boundary conditions reflect (i) a concentration clamped at the channel entrance, representing the well-mixed main channel/reservoir that acts as a sink,

$$C(0,t) = 0, \tag{S11}$$

and (ii) an impermeable dead-end wall imposing a no-flux condition,

$$\left.\frac{\partial C}{\partial x}\right|_{x=L} = 0. \tag{S12}$$

The initial condition corresponds to a uniformly filled dead-end channel,

$$C(x,0) = C_{\text{solute}}. \tag{S13}$$

Under these conditions, separation of variables yields the series solution

$$C(x,t) = \sum_{n=0}^{\infty} \left(\frac{4C_{\text{solute}}}{(2n+1)\pi} \sin\left(\frac{(2n+1)\pi x}{2L}\right) \exp\left[-D\left(\frac{(2n+1)\pi}{2L}\right)^2 t\right]\right). \tag{S14}$$

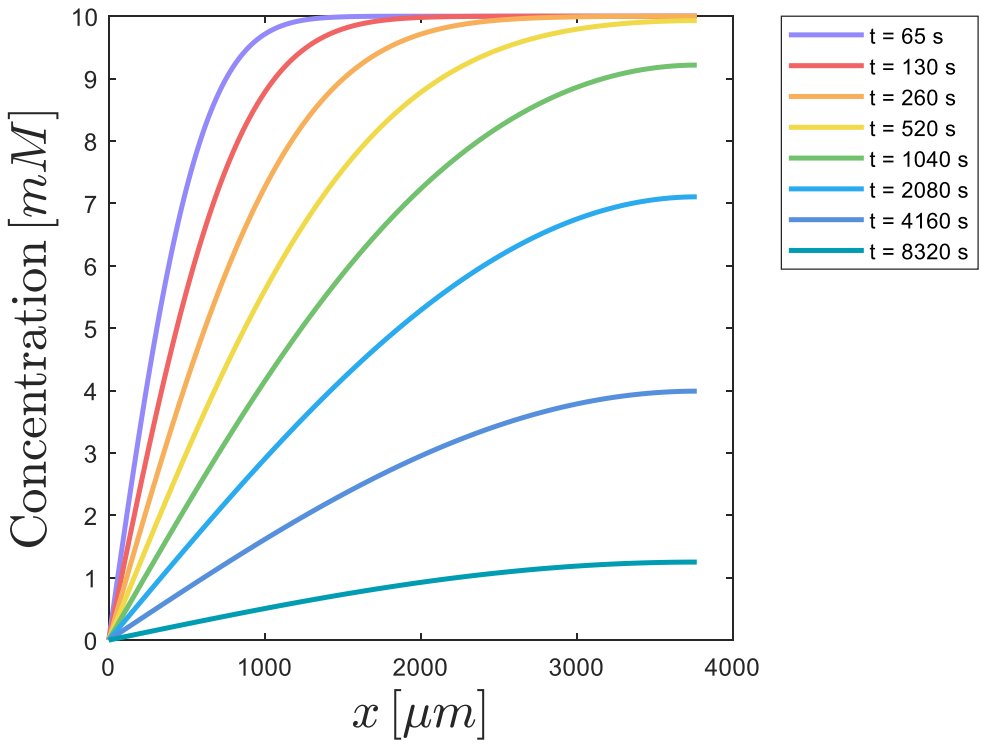

Fig. S3: Concentration profiles of NaCl within the dead-end channel at different times, obtained by solving the one-dimensional diffusion equation. The color gradient represents different time points. An ambipolar diffusion coefficient of $D = 1.61 \times 10^{-9}\,\mathrm{m}^2/\mathrm{s}$ was used in the calculations.

Fig. S3 shows that the NaCl concentration decreases along the length of the dead-end channel over time due to diffusion. Initially steep concentration gradients gradually diminish as the solute diffuses further into the channel. We used an ambipolar diffusion coefficient of $D = 1.61 \times 10^{-9}\,\mathrm{m}^2/\mathrm{s}$ in our calculations, accounting for the combined diffusion of sodium and chloride ions.

Because the dead-end channel is shallow and narrow, transverse diffusion homogenizes the solute rapidly across the cross-section. Using $D = 1.61 \times 10^{-9}\,\mathrm{m}^2/\mathrm{s}$, the transverse diffusion times are $t_h \sim h^2/D \approx 0.1\,\mathrm{s}$ for the channel height ($h = 15\,\mu\mathrm{m}$) and $t_w \sim w^2/D \approx 25$–$40\,\mathrm{s}$ for the channel width ($w \approx 200$–$250\,\mu\mathrm{m}$), which are orders of magnitude smaller than the axial diffusion time $t_L \sim L^2/D \approx 9 \times 10^3\,\mathrm{s}$ for $L \approx 3.77\,\mathrm{mm}$. Therefore, to leading order the solute concentration is uniform in the transverse direction and may be treated as the cross-sectionally averaged field $C(x,t)$. In addition, the dead-end geometry enforces zero net through-flow; any diffusio-osmotically driven motion is primarily recirculating, so advection

contributes only higher-order dispersive corrections to the mean solute profile. Under these conditions, the solute evolution is well approximated by the 1-D diffusion equation.

4 Effect of Channel Height on Critical Position z^*

To evaluate the potential influence of three-dimensional (3D) effects on particle motion within the microfluidic channel, we conducted a theoretical analysis of the bulk flow in the z direction.[6] Specifically, we aimed to determine whether the channel height and the bottom glass substrate could significantly impact the critical reversal position z^* (i.e., the critical position along the height direction).

Using a channel height of 15 μm in our theoretical model for the symmetric PDMS boundary case (as described in the main text), and treating the bottom wall as a glass slide via the corresponding ζ_{glass} from Eq.S6, we calculated the critical vertical position z^*. As shown in Fig. S4, this predicted z^* is considerably smaller than the critical position observed in the width direction. The small z^* in the height dimension suggests that diffusio-osmotic (DO) slip and the associated bulk flow near the top and bottom walls contribute negligibly to particle migration across the channel height.

This conclusion is further supported by experimental observations: across all channel configurations and in all recorded videos (Videos S1–S7), we do not observe particles moving back in the mid-width region (no detectable "return" motion indicative of a significant z-directed DO-driven circulation). Instead, the observed particle reorganization and reversal behavior are consistently confined to the near wall position, indicating that any DO-induced flow component in the z direction is negligible compared to the dominant transport in y.

Therefore, we conclude that three-dimensional effects arising from the channel height are insignificant in this context, and the two-dimensional (2D) analysis presented in the main text adequately captures the essential physics of particle dynamics within the channel.

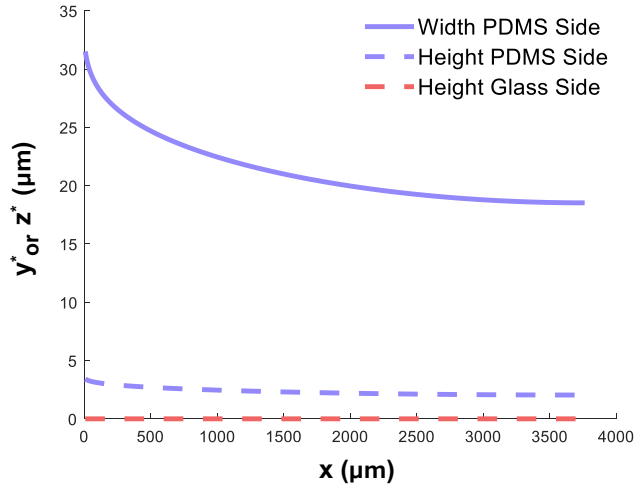

Fig. S4: Comparison of the critical reversal position y^*/z^* between the two-dimensional width case and the three-dimensional height case near different boundary materials.

5 Analysis of the Y-Component of Particle Velocity

Although particle transport in the dead-end channel is primarily along the axial (x) direction, the transverse (y) component of particle velocity provides an additional diagnostic of the local flow structure and any lateral drift induced by boundary conditions. Fig. S5 shows the measured y-component velocities of polystyrene (PS) carboxylate particles at $t = 3557$ s for particles entering from the side channel. Overall, u_y remains close to zero across most of the observation window, indicating negligible lateral migration and confirming that the particle motion is predominantly unidirectional in this geometry.

To obtain u_y, time-lapse fluorescence images were first processed in *ImageJ* to identify particle positions in each frame and to visualize trajectories with time encoded by the color bar. Particle trajectories $(x(t), y(t))$ were then extracted using custom *MATLAB* (MathWorks) routines adapted from Weeks et al.[8] The instantaneous transverse velocity was computed by finite differencing successive positions,

$$u_y(t_i) = \frac{y(t_{i+1}) - y(t_i)}{\Delta t}, \tag{S14}$$

and subsequently averaged over the relevant time window for the snapshot shown in Fig. S5.

To quantify how local velocities vary both along and across the dead-end channel, the

field of view was discretized into rectangular bins of 300 μm in the axial direction and 25 μm in the transverse direction. The mean transverse velocity $\langle u_y \rangle$ within each bin is calculated. Detailed sources of experimental uncertainty in particle detection and velocity estimation, as well as the procedure used to compute the error bars, are provided in the Supporting Information section Experimental Error Sources.

An exception is observed in the convection zone near the dead-end entrance of the channel, where a relatively higher y-velocity profile is detected. In this area, the average y-velocity (V_y) decreases significantly from approximately 0.15 μm/s to 0.01 μm/s as particles move from the convection zone to the region of interest (ROI) in our experiments. Beyond the convection zone, which extends about 500 μm from the channel entrance, the y-component of particle velocities diminishes to levels comparable to fluctuations caused by Brownian motion.

These findings indicate that lateral movements induced by convective effects are confined to the immediate vicinity of the entrance the dead-end channel. The findings are also consistent in the symmetric glued boundary case and the asymmetric PDMS and glue case. Consequently, particles predominantly follow trajectories parallel to the x-axis in the main experimental region.

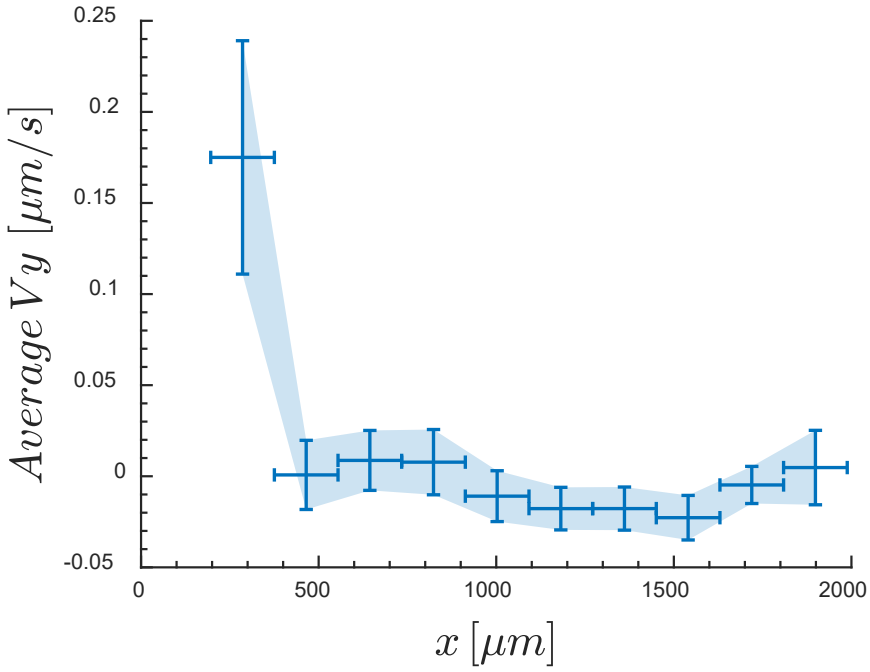

Fig. S5: Y-component of particle velocities for particles in symmetric PDMS boundary conditions at 3557 seconds from particle flowing in the side channel. The shaded area represents the standard error calculated based on the number of particles in each measurement. The significant reduction in v_y from the convection zone toward the ROI highlights the minimal lateral movement of particles in the main flow region.

6 Validation of Diffusiophoresis

To confirm that particle movement in our experiments is driven by diffusiophoresis and not other factors, we conducted control experiments without a salt concentration gradient. In these tests, both the dead-end channel and the main channel were filled with Milli-Q (MQ) water. A particle suspension prepared in MQ water was introduced into the main channel. As shown in Fig. S6(a), under these conditions, particles did not enter the dead-end channel, indicating no significant particle movement without a solute gradient.

In contrast, when we established a salt concentration gradient by filling the dead-end channel with a 10 mM NaCl solution while keeping the particle suspension in MQ water, particles began to migrate into the dead-end channel (Fig. S6(b)). This migration confirms that the presence of a solute concentration gradient induces particle movement via diffusiophoresis and diffusio-osmosis, consistent with observations from previous studies.

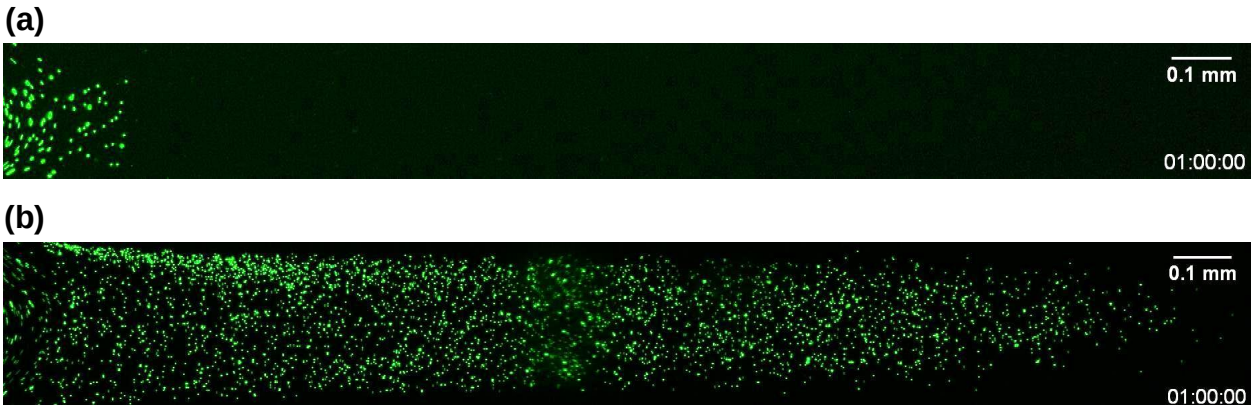

Fig. S6: Overlaid microscope images of the dead-end channel from $t = 0\,\mathrm{s}$ to $t = 3600\,\mathrm{s}$. (a) Control experiment: both the dead-end channel and the particle suspension contain Milli-Q water; particles do not enter the dead-end channel. (b) Experiment with a salt concentration gradient: the dead-end channel contains 10 mM NaCl while the particle suspension is in Milli-Q water; particles migrate into the dead-end channel due to diffusiophoresis. Scale bar: $100\,\mu\mathrm{m}$.

7 Width Uniformity of the UV-Glue and Its Impact on Channel Geometry

Because UV-cured glue is used to tune the microchannel zeta potential, it is important to clarify whether the coating changes the dead-end channel width and how uniform the coating is along the channel. The symmetric PDMS and symmetric-glue devices were fabricated with a designed channel width of approximately $200\,\mu\mathrm{m}$ (using 3D-printed molds and PDMS molds via conventional soft lithography and microfluidic sticker techniques). The asymmetric device was intentionally designed wider (approximately $250\,\mu\mathrm{m}$) and then coated on one side with UV glue so that the effective channel width, w_{eff}, remains close to the $200\,\mu\mathrm{m}$ target.

To quantify the geometric impact of the UV-glue coating, we measured the glue width $W(x)$ along the dead-end channel from brightfield microscopy images (Fig. S7a,b). Here, W is defined as the lateral distance from the coated wall to the glue–channel interface. Over the imaged length of 3.2 mm, the coating is continuous and $W(x)$ remains in the range of approximately 40–60 μm (mean $\sim 50\,\mu\mathrm{m}$) with an axial variation of about $\pm 10\,\mu\mathrm{m}$. This implies

$$w_{\mathrm{eff}}(x) \approx 250\,\mu\mathrm{m} - W(x) \approx 190\text{–}210\,\mu\mathrm{m}, \tag{1}$$

This bounded width variation produces only a small uncertainty in the transport metrics derived from our model. Specifically, the model predicts that the width-normalized critical

position is width-independent as shown in Eq.20 in the main text,

$$\frac{y^*}{w} = f\Big(\frac{x}{L}\Big) \quad , \tag{2}$$

so that

$$y^*(x) = w_{\text{eff}}(x)\, f\Big(\frac{x}{L}\Big)\,. \tag{3}$$

Therefore, using a nominal width $w_{\text{nom}} = 200\,\mu$m while the measured effective width satisfies $w_{\text{eff}} = 200 \pm 10\,\mu$m introduces only a $\pm 5\%$ multiplicative uncertainty in y^*/w_{nom} (approximately 10% peak-to-peak). This uncertainty preserves the functional dependence on x/L and is within the experimental error. We illustrate this bounded sensitivity in Fig. S7c as a narrow band corresponding to a 10% width difference.

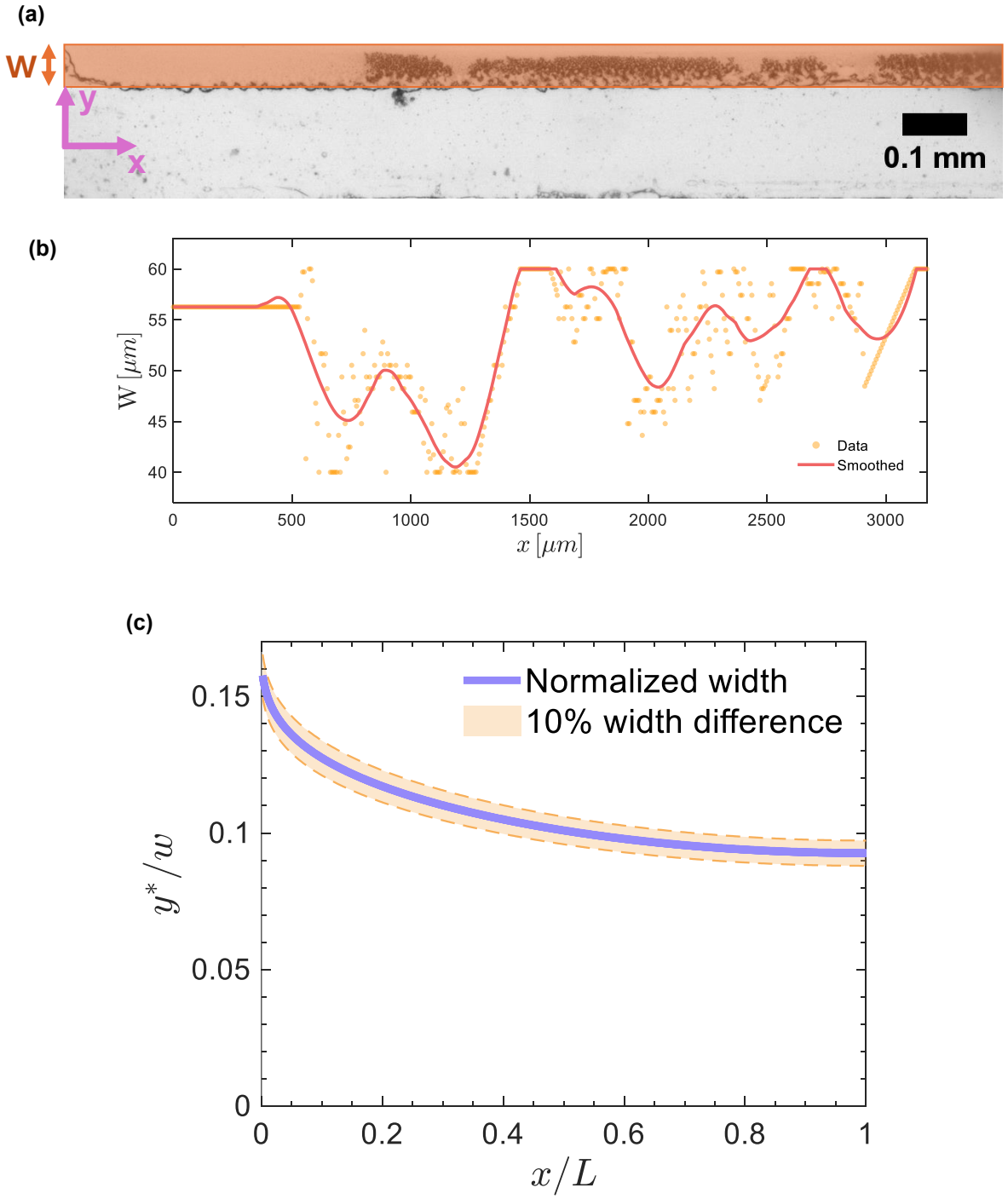

Fig. S7: Quantification of the width uniformity of the UV-glue coating in the asymmetric dead-end channel. (a) Representative brightfield microscopy image of the UV-glue-coated region along one sidewall of the dead-end channel (highlighted). The lateral glue width W is defined as the distance from the coated wall to the glue–channel interface (arrow). Scale bar: 0.1 mm. (b) Extracted coating-width profile $W(x)$ along the axial direction x over a 3.2 mm imaged length. Points show measurements and the curve shows a smoothed trend. (c) Predicted sensitivity of the normalized critical position y^*/w to a 10% width difference, shown as a narrow band around the nominal curve, indicating that modest residual width variation produces only a small multiplicative change without altering the functional dependence on x/L.

8 Example Particle Tracks Near Symmetric and Asymmetric Boundaries

To illustrate the impact of boundary materials on particle motion within the dead-end channels, we present example particle tracks observed under different boundary conditions. We implemented the built-in MTrackJ plugin in ImageJ software to track single particles as shown in Fig. S8 and Fig. S9.[7]

In Fig. S8, we display particle trajectories in dead-end pores with symmetric boundaries:

- **Fig. S8(a):** Particle motion near symmetric PDMS boundaries.
- **Fig. S8(b):** Particle motion near symmetric NOA-81 UV glue boundaries.

Fig. S8(c) and S8(d) highlight the critical reversal positions y^* for PDMS and glue boundaries, respectively. It is evident that y^* near the glue boundaries is significantly smaller than that near PDMS boundaries. This difference arises because the smaller zeta potential of the UV glue results in a weaker diffusio-osmotic flow, leading to a reduced bulk flow effect on particle movement.

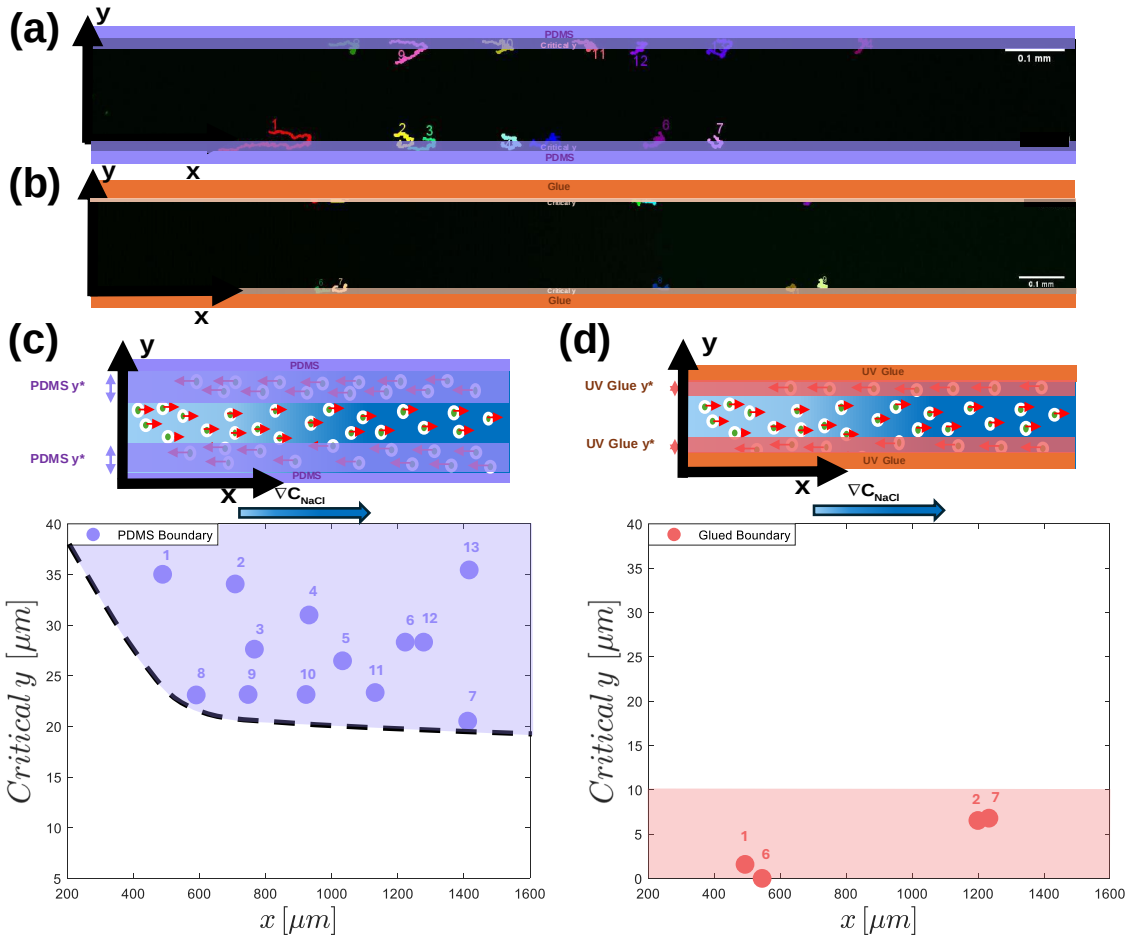

Fig. S8: Example particle tracks in dead-end channels with symmetric boundaries. (a) Particle motion near symmetric PDMS boundaries. (b) Particle motion near symmetric NOA-81 UV glue boundaries. (c) Illustration of the critical reversal position y^* near PDMS boundaries. (d) Illustration of y^* near glue boundaries. The smaller y^* near glue boundaries is due to the weaker zeta potential of the UV glue, resulting in a smaller bulk flow effect.

Fig. S9 shows particle tracks in a dead-end pore with asymmetric boundaries:

- **Fig. S9(a):** Particle motion near the PDMS boundary.
- **Fig. S9(b):** Particle motion near the NOA-81 UV glue boundary.

Fig. S9(c) compares the critical reversal positions y^* on both sides. Consistent with the symmetric case, y^* near the glue boundary is noticeably smaller than that near the PDMS boundary due to the lower zeta potential of the glue, which diminishes the bulk flow effect and affects particle reversal positions.

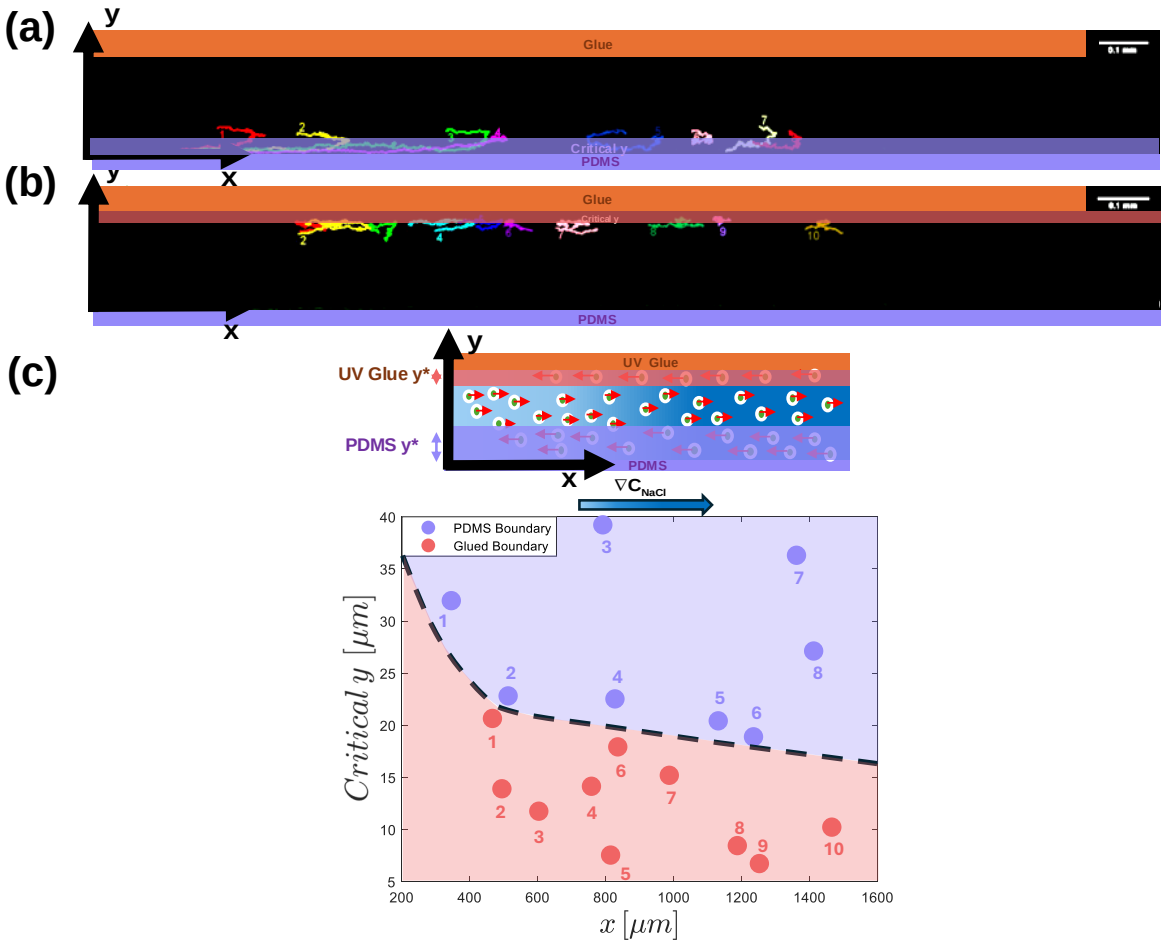

Fig. S9: Example particle tracks in dead-end channels with asymmetric boundaries. (a) Particle motion near the PDMS boundary. (b) Particle motion near the NOA-81 UV glue boundary. (c) Comparison of the critical reversal positions y^* near PDMS and glue boundaries. The smaller y^* near the glue boundary is due to its lower zeta potential, leading to a reduced bulk flow effect on particle movement.

These observations reinforce the conclusion that the material properties of the channel walls significantly influence particle dynamics through their effect on zeta potentials and, consequently, diffusio-osmotic flows. By selecting appropriate wall materials, one can control the critical reversal position y^* and optimize particle transport within microfluidic devices.

9 Videos S1 to S7

Videos S1–S3 correspond to Fig. 3, which illustrates particle transport in dead-end channels with (i) symmetric PDMS boundaries, (ii) symmetric UV-glue boundaries, and (iii) asymmetric PDMS/UV-glue boundaries. Videos S4–S7 correspond to Figs. S7 and S8, which show representative particle trajectories in dead-end channels with symmetric PDMS boundaries,

symmetric UV-glue boundaries, and asymmetric PDMS/UV-glue boundaries.

All videos are displayed at 240× playback speed (0–15 s), and the scale bar represents 100 μm.

References

[1] Kirby, B. J.; Hasselbrink, E. F. Zeta potential of microfluidic substrates: 2. Data for polymers. *Electrophoresis* **2004**, *25*, 203–213.

[2] Feng, Y.; Goree, J.; Liu, B. Errors in Particle Tracking Velocimetry with High-Speed Cameras. *Review of Scientific Instruments* **2011**, *82*, 053707.

[3] Raffel, M.; Kähler, C.; Willert, C.; Wereley, S.; Scarano, F.; Kompenhans, J. *Particle Image Velocimetry: A Practical Guide*; 3rd ed.; Springer: Germany, 2018.

[4] Akdeniz, B.; Wood, J. A.; Lammertink, R. G. H. Diffusiophoresis and Diffusio-osmosis into a Dead-End Channel: Role of the Concentration-Dependence of Zeta Potential. *Langmuir* **2023**, *39*, 6, 2322–2332.

[5] Ault, J. T.; Warren, P. B.; Shin, S.; Stone, H. A. *Diffusiophoresis in One-dimensional Solute Gradients*; Soft Matter **2017**, *13*, 9015–9023.

[6] Alessio, B. M.; Shim, S.; Mintah, E.; Gupta, A.; Stone, H. A. *Diffusiophoresis and Diffusioosmosis in Tandem: Two-dimensional Particle Motion in the Presence of Multiple Electrolytes*; Phys. Rev. Fluids **2021**, *6*, 054201.

[7] Meijering, E.; Dzyubachyk, O.; Smal, I. Methods for Cell and Particle Tracking. *Methods in Enzymology* **2012**, *504*, 183–200.

[8] Weeks, E. R.; Crocker, J. C. Particle Tracking Using IDL. *Online resource* **2012**. Tracking kit last updated May 25, 2012; accessed December 22, 2025. Available at: `https://faculty.college.emory.edu/sites/weeks/idl/`.

[9] Gu, Y.; Li, D.-D. The Zeta Potential of Glass Surface in Contact with Aqueous Solutions. *Journal of Colloid and Interface Science* **2000**, *226*, 2, 328–339. DOI: `10.1006/jcis.2000.6827`.